Biomaterials 104 (2016) 182–191

Contents lists available at ScienceDirect

Biomaterials

journal homepage: www.elsevier.com/locate/biomaterials

In vivo biodistribution studies and *ex vivo* lymph node imaging using heavy metal-free quantum dots

Elnaz Yaghini [a, *], Helen D. Turner [b], Alix M. Le Marois [c], Klaus Suhling [c], Imad Naasani [b], Alexander J. MacRobert [a]

[a] Division of Surgery and Interventional Science and Institute of Healthcare Engineering, University College London, London, UK
[b] Nanoco Technologies Ltd., 46 Grafton Street, Manchester, UK
[c] Department of Physics, King's College London, London, UK

ARTICLE INFO

Article history:
Received 25 January 2016
Received in revised form
8 June 2016
Accepted 10 July 2016
Available online 12 July 2016

Keywords:
Nanoparticles
Heavy metal-free quantum dots
Breast cancer
Sentinel lymph node
Nanotechnology
Photoluminescence

ABSTRACT

Quantum dots (QDs) are attractive photoluminescence probes for biomedical imaging due to their unique photophysical properties. However, the potential toxicity of QDs has remained a major obstacle to their clinical use because they commonly incorporate the toxic heavy metal cadmium within the core of the QDs. In this work, we have evaluated a novel type of heavy metal-free/cadmium-free and biocompatible QD nanoparticles (bio CFQD® nanoparticles) with a good photoluminescence quantum yield. Sentinel lymph node mapping is an increasingly important treatment option in the management of breast cancer. We have demonstrated their potential for lymph node mapping by *ex vivo* imaging of regional lymph nodes after subcutaneous injection in the paw of rats. Using photoluminescence imaging and chemical extraction measurements based on elemental analysis by inductively coupled plasma mass spectroscopy, the quantum dots are shown to accumulate quickly and selectively in the axillary and thoracic regional lymph nodes. In addition, lifetime imaging microscopy of the QD photoluminescence indicates minimal perturbation to their photoluminescence properties in biological systems.

1. Introduction

Many cancers metastasise via the lymphatic system, therefore the presence of lymph node metastasis is an important prognostic marker in many cancers including melanoma, breast, colon, lung and ovarian cancers [1,2]. Breast cancer cells are most likely to spread to the lymph nodes (LNs) located in the axilla, therefore accurate assessment of the axillary lymph nodes (ALN) is the most prognostic indicator of survival and recurrence in patients with (early-stage) breast cancer. Axillary lymph node dissection (ALND) has long been used for the management of the breast cancer. However, ALND is associated with considerable short and long-term morbidities such as seroma formation, impairment of shoulder motion, numbness, paresthesias, nerve injury, wound infection, and arm lymphoedema. In addition patients must stay in hospital for longer with significant cost implications. Moreover, most patients with early-stage breast cancer are node negative, and ALND exposes them to the potential side effects of this procedure with no benefit [3–5].

These complications have led to the concept of sentinel lymph node biopsy (SLNB) as a minimally invasive procedure used for staging melanoma and breast cancer and its use is being studied for other types of solid cancers [6–8]. A sentinel lymph node (SLN) is defined as the first lymph node(s) to receive lymphatic drainage from the site of a tumour. With this method, SLN can be identified using tracer agents (e.g radiolabelled colloid, and or vital blue dye) which are injected around the primary tumour site. After a few minutes the axilla is minimally incised, and stained lymphatic vessels and stained lymph nodes are detected visually. The combination of radioactive lymphatic tracers and blue dye staining

Abbreviations: LNs, lymph nodes; ALN, axillary lymph node; ALND, Axillary lymph node dissection; SLNB, sentinel lymph node biopsy; SLN, sentinel lymph node; NPs, nanoparticles; ICG, indocyanine green; NIR, near-infra red; QD, quantum dot; QY, quantum yield; PL, photoluminescence; RES, reticuloendothelial system; HF, hydrofluoric acid; PEG, polyethylene glycol; TEM, transmission electron microscopy; DLS, dynamic light scattering; TLN, thoracic lymph node; LED, light-emitting diode; LALN, left axillary lymph node; LTLN, left thoracic lymph node; ICP-MS, inductively coupled plasma-mass spectroscopy; FLIM, fluorescence lifetime imaging; CCD, charge-coupled device; MA, myristic acid; TMS, trimethylsilyl; HF, hydrofluoric acid.

* Corresponding author.
E-mail address: elnaz.yaghini@ucl.ac.uk (E. Yaghini).

http://dx.doi.org/10.1016/j.biomaterials.2016.07.014

increases the success and accuracy of the SLN mapping [9–13].

Although blue dyes are straightforward, inexpensive and safe to use, their efficiency in identifying SLNs is limited. Blue dye molecules (e.g., Patent Blue V, Evans blue, methylene blue) are too small and migrate quickly from the SLN to the entire lymphatic system. As a result, the prolonged preparation time increases blue staining of secondary, third and sequential nodes. Therefore, surgical skill and experience are required to locate and remove the SLNs before the dye spreads to other nodes. The dyes have also been reported to cause various allergic reactions in patients such as rush, erythaema and anaphylactic reaction [14,15]. With the radioactive tracing approach, specific techniques, equipment (Gamma camera) and training are needed to minimise the hazard to patients and staff. Close collaboration with a licensed nuclear medicine facility is required, incurring logistical and waste disposal problems [16,17].

The use of iron oxide nanoparticles (NPs) detected with a handheld magnetometer probe is another approach which has been used to identify the SLN [18–21]. With this approach, the SLN can be identified using the point-source magnetometer probe but imaging requires MRI scanning. Moreover, the surgeon cannot use metallic surgical instruments with these techniques.

Fluorescent agents administered locally or systemically are used extensively for preclinical *in vivo* imaging and increasingly for image-guided surgery in human patients. Fluorescent organic molecules and nanoparticles offer an alternative approach to conventional lymphotropic agents of the SLN mapping, to enable transcutaneous real-time lymphography and intraoperative lymph node detection. One of the currently approved fluorescent contrast agents by the FDA for clinical applications is indocyanine green (ICG), which has been widely used in clinical research due to its near-infra red (NIR) fluorescent emission which entails low autofluorescence and increased tissue transparency [22,23]. The use of ICG for the visualisation of the lymphatic mapping was first described by Motomura et al., in 1999 [24]. ICG has been used as the lymphatic tracer for SLN mapping in breast cancer, gastric cancer, and colon cancer. However, as with the blue dyes, ICG is rapidly cleared through the sentinel node to second-tier nodes eventually spreading to the subcutaneous tissue, and its relatively low fluorescence quantum yield (QY) and rapid photobleaching limit ICG's usefulness for intraoperative SLN mapping [25].

Semiconductor quantum dot (QD) nanoparticles have attracted much attention over the past few years as a novel class of luminescence probes for many biological and biomedical applications [26–29]. The main advantages for the use of QDs as bioimaging probes are their photophysical properties such as high photoluminescence (PL) quantum yield, high photobleaching threshold, size and composition-dependent tunable photoluminescence that can span the entire spectrum and high photostability compared to organic dyes [30,31]. They have therefore become promising alternatives to organic fluorophores in many applications particularly as probes for biomedical imaging [32].

One of the first uses of QDs *in vivo* was mapping the reticuloendothelial system (RES) and locating draining lymph nodes [33,34]. Ballou et al. were amongst the first to inject the QDs into the tumours to map SLNs [33]. They demonstrated that tumour injection of QDs resulted in rapid migration of QDs from the tumour through lymphatics to surrounding lymph nodes which were visible through the skin. Frangioni and colleagues used NIR emitting CdTe/CdSe core/shell QDs and demonstrated SLN mapping of QDs when injected intradermally into the paw of a mouse [34]. They also injected NIR QDs intradermally on the thighs of pigs and followed lymphatic flow towards the SLN in real time [34]. Since the first examples from Ballou's and Frangioni's groups a significant amount of effort has been applied to investigate the potential of QDs as luminescence probes for SLN mapping [35–41]. Preliminary data and studies suggest that SLN detection guided by QD nanoparticles could emerge as a new method for SLN mapping. However, one major drawback that severely hinders the clinical translation of QDs is the inherent toxicity of the individual ions (such as Cd^{2+}, Se^{2-} and Te^{2-}) that the dots contain, particularly Cd^{2+} [42–44]. For instance in study by Marchal et al. the detection of the SLN and the toxicity of the cadmium-containing QDs (CdTeSe/CdZnS) were compared with cadmium-free counterparts ($CuInS_2$/ZnS) [45]. They also noted that the cadmium-based QDs clearly showed signs of toxicity, with inflammation evident in resected regional lymph nodes. However, the cadmium-free QDs did not show any signs of toxicity under the same conditions. Therefore, in recent years several groups have been interested in the fabrication of cadmium-free QDs for biological applications [46–48].

QDs made up of III–V semiconductor nanocrystals (such as InP) are appropriate candidates as they do not have class A or B elements and also structurally are more robust owing to the presence of covalent bonds in their matrix [49,50]. Indium-based QDs are therefore a promising substitute for cadmium-based QDs for biological studies. Several other core-shell combinations including indium for Cadmium-free QDs have been investigated successfully for *in vivo* imaging [51,52].

Nevertheless, relatively few studies have reported the use of indium-based QDs in biomedical applications, since the synthetic procedure for preparing indium-based QDs is more complicated than cadmium-based QDs. The aim of our study was to demonstrate the applicability and effectiveness of new biocompatible water soluble indium-based QDs (bio CFQD® nanoparticles, Nanoco Technologies Ltd.) and investigate their applicability for *in vivo* axillary lymphatic mapping.

2. Materials and methods

2.1. Synthesis of bio CFQD® nanoparticles

Bio CFQD® nanoparticles based on indium (In) compositions were manufactured in the laboratories of Nanoco Technologies Ltd., Manchester, UK using proprietary synthetic procedures following the patented molecular seeding process [53].

Briefly, the preparation of crude (non functionalised) indium-based quantum dots with emission in the range of 500–700 nm was carried out as follows: Dibutyl ester (approximately 100 mL) and myristic acid (MA) (10.06 g) were placed in a three-neck flask and degassed at ~70 °C under vacuum for 1 h. After this period, nitrogen was introduced and the temperature was increased to ~90 °C. Approximately 4.7 g of the ZnS molecular cluster $[Et_3NH_4][Zn_{10}S_4(SPh)_{16}]$ was added, and the mixture was stirred for approximately 45 min. The temperature was then increased to ~100 °C, followed by the drop-wise additions of In $(MA)_3$ (1 M, 15 mL) followed by $(TMS)_3P$ (1 M, 15 mL). The reaction mixture was stirred while the temperature was increased to ~140 °C. At 140 °C, further drop-wise additions of In $(MA)_3$ dissolved in di-*n*-butylsebacate ester (1 M, 35 mL) (left to stir for 5 min) and $(TMS)_3P$ dissolved in di-*n*-butylsebacate ester (1 M, 35 mL) were made. The temperature was then slowly increased to 180 °C, and further drop-wise additions of In $(MA)_3$ (1 M, 55 mL) followed by $(TMS)_3P$ (1 M, 40 mL) were made. By addition of the precursor in this manner, indium-based particles with an emission maximum gradually increasing from 500 nm to 720 nm were formed. The reaction was stopped when the desired emission maximum was obtained and left to stir at the reaction temperature for half an hour. After this period, the mixture was left to anneal for up to approximately 4 days (at a temperature ~20–40 °C below that of the reaction). A UV lamp was also used at this stage to aid in annealing. The particles

were isolated by the addition of dried degassed methanol (approximately 200 mL) via cannula techniques. The precipitate was allowed to settle and then methanol was removed via cannula with the aid of a filter stick. Dried degassed chloroform (approximately 10 mL) was added to wash the solid. The solid was left to dry under vacuum for 1 day. This procedure resulted in the formation of indium-based nanoparticles on ZnS molecular clusters. In post-operative treatments, the quantum yields of the resulting indium-based nanoparticles were further increased by washing in dilute hydrofluoric acid (HF). The quantum efficiencies of the indium-based core material ranged from approximately 25%–50%.

Growth of a ZnS shell: A 20 mL portion of the HF-etched indium-based core particles was dried in a three-neck flask. 1.3 g of myristic acid and 20 mL di-*n*-butyl sebacate ester were added and degassed for 30 min. The solution was heated to 200 °C, and 2 mL of 1 M $(TMS)_2S$ was added drop-wise (at a rate of 7.93 mL/h). After this addition was complete, the solution was left to stand for 2 min, and then 1.2 g of anhydrous zinc acetate was added. The solution was kept at 200 °C for 1 h and then cooled to room temperature. The particles were isolated by adding 40 mL of anhydrous degassed methanol and centrifuging. The supernatant liquid was discarded, and 30 mL of anhydrous degassed hexane was added to the remaining solid. The solution was allowed to settle for 5 h and then centrifuged again. The supernatant liquid was collected and the remaining solid was discarded. The quantum efficiencies of the final unfunctionalised (crude) indium-based nanoparticle material ranged from approximately 60%–90% in organic solvents.

Water solubilisation and surface functionalisation of the crude nanoparticles was achieved using a proprietary method based on surface crosslinking with hexamethoxymethylmelamine (HMMM) [54]. The details of this method of functionalisation will be described in a separate publication. Briefly, a toluene solution of crude nanoparticles was refluxed under nitrogen in the presence of amphiphilic ligands and polyethylene glycol (PEG). Following several hours of reflux, the toluene was removed by evaporation and then the product was reconstituted in deionised H_2O. The aqueous solution of dots was purified by several cycles of ultrafiltration using 30kD centrifugation ultrafilters. The dots were grafted with PEG to increase solubility of the nanoparticles and to prolong their blood-half-life by reducing their reticuloendothelial system (RES) uptake [55,56]. The water soluble surface treated nanoparticles (bio CFQD®) displayed relatively high photoluminescence quantum yields (0.35–0.45) in aqueous buffers (pH 5–8) and were stable for at least several months in water with negligible PL loss or precipitation.

2.2. Characterisation of bio CFQD® nanoparticles

Transmission electron microscopy (TEM) analysis was challenging due to the low electron density nature of the particles. Fig. 1 (A and B) shows a typical TEM image and the size distribution of a typical sample of the bio CFQD® nanoparticles. The TEM images were acquired using a JEOL 2010 analytical TEM. The hydrodynamic particle size was determined by the measurement of dynamic light scattering (DLS) using a Malvern Zetasizer μV system. The nanoparticles were dispersed in aqueous buffer (HEPES 6 mM, pH 7.8). The average hydrodynamic size of the surface-treated water soluble particles (bio CFQD®) is 12.2 nm with a standard deviation of 0.29 nm (Fig. 1C).

Fig. 1D shows the photoluminescence emission spectrum of the bio CFQD® nanoparticles in distilled water, which shows peak emission at 615 nm. The photoluminescence emission spectrum of QDs was recorded using a fibre optic CCD spectrometer (USB4000, Ocean Optics Inc.). For the quantum yield measurement a spectrometer incorporating an integrating sphere was used (Hamamatsu UK. Ltd, model C9920-02), which has been specifically designed to measure absolute quantum yields.

2.3. Cell culture

MCF-7 cell line (human breast adenocarcinoma) was obtained from Sigma-Aldrich. The cells were grown in DMEM-F12 medium containing 10% FCS. All culture flasks were kept inside a humidified incubator at 37 °C and 5% CO_2.

2.4. In vitro toxicity test

The effect of bio CFQD® nanoparticles on viability of MCF-7 cells was evaluated with the use of the MTT viability assay. Briefly, cells were seeded on each well of 96-well-plate at a density of 5×10^3 and cultured in a humidified 5% CO_2 incubator at 37 °C for 24 h. The next day, the culture medium was removed and was replaced with fresh cell culture medium containing various concentrations of QDs (12.5–200 nM). Cells without QDs were used as the control. Cell viability was measured after 24 and 48 h incubation using the MTT assay. Experiments were carried out in triplicate. Following incubation with the QDs, the culture medium was removed and 100 μL of MTT (1 mg/mL) was added into each well and incubated at 37 °C for 2 h. The water-insoluble formazan crystals were solubilised with dimethyl sulfoxide (DMSO) and the optical density (OD) of each well at 565 nm was recorded on a microplate reader (BioTek Instruments Inc.)

2.5. Animal experiments

150–175 g female Hooded Lister rats were purchased from Harlan UK Ltd and acclimatised to the animal facility for 7 days prior to experimentation. Animals were kept in 12 h light/dark cycles and had free access to food and water. All procedures were carried out with Home Office licence approval.

2.6. Haemolysis test

Fresh red blood cells (RBC) obtained from rats were suspended in physiological saline (0.9% sodium chloride) (negative control), deionised water (positive control) or various bio CFQD® nanoparticles dilutions in sodium chloride, ranging from 12.5 to 200 nM. The solutions were incubated for 3 h at 37 °C before centrifugation. 100 μL of the supernatant was transferred to a 96 well-plate. The absorbance of the supernatant at 565 nm was recorded with a microplate reader (BioTek Instruments Inc.). Experiments were carried out in triplicate. The haemolysis of RBC (%) was calculated as ((absorbance of sample − absorbance of negative control)/(absorbance of positive control-absorbance of negative control)) x 100 [57,58].

2.7. Ex vivo imaging

An aqueous solution of the QDs in PBS was injected subcutaneously into the left paw of rats at 30 pmol/g of body weight, corresponding to a dose of 7.5 mg/kg body weight. Rats were killed 10 min post-injection, and an incision was made to expose the axillary lymph node (ALN) and thoracic lymph node (TLN) for *ex vivo* imaging. The axillary area was illuminated with a collimated light-emitting diode (LED) lamp (Thorlabs Inc. model M455L2) with peak emission at 455 nm and an incident power density on the sample of 3 mW/cm^2. Photoluminescence was imaged using a Peltier-cooled 12 bit single chip 680 × 480 pixel charge-coupled device (CCD) colour camera (Sensicam, PCO, Germany) incorporating a red/green/blue (RGB) mosaic filter. The images were captured by a frame-grabber and images were analysed using ImageJ.

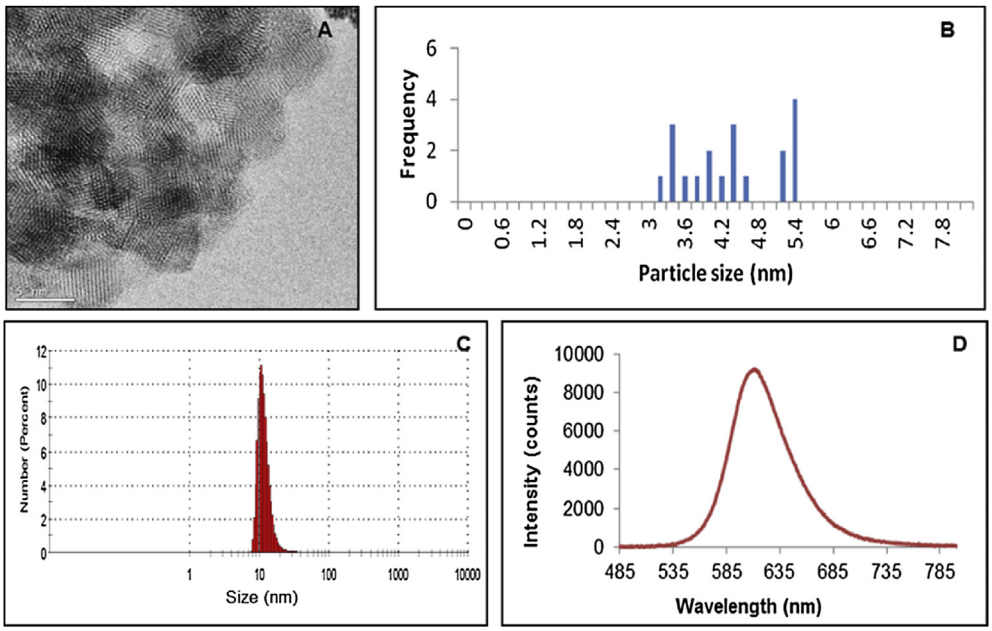

Fig. 1. (A and B) TEM image (scale bar corresponds to 5 nm) and size distribution of bio CFQD® nanoparticles from TEM, (C) hydrodynamic size of surface-treated bio CFQD® nanoparticles using DLS, (D) Photoluminescence emission spectrum of an aqueous solution of water soluble bio CFQD® nanoparticles (1 μM) using excitation at 405 nm.

Excised lymph nodes were individually imaged in a separate set of experiments. Rats were again administered with QDs at 30 pmol/g of body weight, and the animals were sacrificed at various times post-injection. The ALN and TLN were removed, tissues were placed adjacently on anodised aluminium plates and were illuminated with a collimated LED lamp at 455 nm. Rats which received only PBS were used as controls. Photoluminescence images of the QDs in excised tissue specimens were recorded using a 16 bit Peltier-cooled 512 × 512 pixel charge-coupled device (CCD) camera (PIXIS 512F, Princeton Instruments Inc.) equipped with a short-working distance lens. Photoluminescence was recorded via a bandpass filter centred at 620 nm (620DF40, Omega Optical Inc.). The system was controlled by a PC computer using WinSpec software (Princeton Instruments Inc.), which processed the 16 bit images.

2.8. Microscopic localisation studies

Rats were administered with 30 pmol/g of body weight of the QDs, as described in the previous section. Animals were killed 5 min, 1 h, 4 h, 48 h, 5 days and 10 days post-injection and the axillary and thoracic lymph nodes were harvested for microscopic imaging of QD photoluminescence. The harvested tissues were first frozen by contact with an isopentane slush and stored at −80 °C prior to use. Five consecutive 10 μm thick tissue sections from tissue block mounted with OCT Embedding Medium (Raymond A. Lamb, UK) were cut from each sample and placed on clean glass slides. Photoluminescence from the cryosections was recorded using an inverted epifluorescence microscope (Olympus IMT-2) equipped with a 16 bit Peltier cooled 512 × 512 pixel CCD camera (Princeton Instruments, model PIXIS 512 F). QD excitation was provided by a 405 nm laser diode module (Laser Components UK, Ltd). The filter set for the phosphorescence imaging consisted of a 500 nm cut-on dichroic mirror (Omega Optical Inc. 500 AGSP), and a long pass filter (Schott RG570) together with a 40 nm bandpass emission filter centred at 620 nm close to the peak emission of the QDs (Omega Optical Inc., 620DF40). After recording the images, selected slides were stained with haematoxylin and eosin (H & E) to identify microscopic localisation of QDs, and imaged with a NanoZoomer digital slide scanner (Hamamatsu Inc.). An area from the stained section was then recorded at the same tissue site identified from the corresponding stored photoluminescence image.

2.9. Biodistribution and pharmacokinetic studies

Nine groups of animals each composed of 3 rats were used for the pharmacokinetic studies. One group served as the control group and rats were injected subcutaneously into the paw with 100 μL of PBS. The other 8 groups were injected with 100 μL of QD solution at a concentration of 30 pmol/g of body weight. The rats were sacrificed at 1 h, 4 h, 24 h, 72 h, 10 days, 30 days, 60 days and 90 days and blood and various organs were collected for the pharmacokinetic study.

2.10. Quantification of uptake in organs

Various organs (the axillary lymph node, thoracic lymph node, brain, thymus, lung, heart, liver, spleen, kidneys, colon, injection site and blood) were collected, weighed and stored in a −80 °C freezer prior to use. For the quantification of QDs in organs, 0.1 g of each tissue in triplicate was prepared and digested by the addition of 1 mL 70% nitric acid (HNO_3). Samples were incubated with 70% nitric acid overnight. The next day the samples were heated in a water bath at 90 °C for 4 h. Later, the samples were cooled at room temperature and re-diluted by adding 5 mL distilled deionised water. Afterwards, the samples were filtered using 0.45 μm pore poly (vinylidene fluoride) membrane syringe filters. The indium (In) ion content was quantified with inductively coupled plasma-mass spectroscopy (ICP-MS) (PerkinElmer SCIEX ICP mass spectrometer, ELAN DRC 6100, USA) to determine the total indium in the organs. For all ICP-MS measurements, nitric acid blank, blank tissue samples, spiked samples with known QDs for calibration and indium standards were prepared and tested concurrently with test samples [59]. The tissues from the control rats without QD administration were dissolved in a similar manner.

2.11. Ex vivo FLIM imaging of QDs in lymph nodes and in aqueous solution

To investigate the stability of the quantum dots under *in vivo* conditions, photoluminescence lifetime of QDs in aqueous solution and the harvested axillary and thoracic lymph nodes were measured using the fluorescence lifetime imaging technique (FLIM). Animals were injected using the same protocol as in the biodistribution studies. Freshly excised lymph node samples, including controls without QD, were placed in a small Petri dish incorporating a thin glass coverslip bottom (Fluorodish, World Precision Inst. Ltd.) which was placed on the stage of an inverted microscope (model TCS SP2, Leica Microsystems Ltd.). A 63× water immersion objective was used to image the samples which were excited with a pulsed picosecond diode laser emitting at 470 nm at 1 MHz repetition rate (Hamamatsu Photonics KK, Japan, model PLP-10, 90 ps pulse duration). Lifetime mapping was measured using a Time-Correlated Single Photon Counting (TCSPC) FLIM system (Becker and Hickl GmbH, Germany, model SPC150). Photoluminescence of QDs was collected via a bandpass filter centred at 620 nm (620DF40, Omega Optical Inc.). The 512 × 512 pixel images were analysed using SPC Image software (Becker & Hickl GmbH, Germany).

3. Results and discussion

3.1. Cellular toxicity

The biocompatibility of the QDs was evaluated using a standard viability assay and a haemolysis assay. Fig. 2 shows that after 24 h of incubation with bio CFQD® nanoparticles negligible changes were recorded vs. untreated control cells. In the case of prolonged exposure (48 h) no significant reduction in cell viability was detected for QD-treated cells at concentrations as high as 200 nM confirming the good biocompatibility of bio CFQD® nanoparticles. Similar results were obtained using SKOV-3 cells (human ovarian cancer cells) incubated with bio CFQD® nanoparticles (data not shown). The data presented here with bio CFQD® nanoparticles compares favourably with other studies using cadmium-free QDs [41,48,60]. It should be noted that lower toxicity may also arise from the surface coating as well as the core/shell composition of the QDs, so it is difficult to discern the relative contributions of these and other factors [61]. However, Brunetti et al. compared the toxicity of InP/ZnS and CdSe/ZnS QDs in each case capped with mercaptopropionic acid towards A459 human lung carcinoma cells and other cell lines and concluded that leaching of cadmium ions was the main factor responsible for the significantly higher toxicity of the cadmium-containing QDs [48].

3.2. Haemolysis test

Haemolytic properties are commonly used as a realiable technique to test the biocompatibility of nanoparticles under *in vitro* conditions [57,58]. In this study, the biocompatibility of bio CFQD® nanoparticles was carried out by investigating the extent of haemolysis over a broad concentration range (12.5–200 nM) following incubation for 3 h. The bio CFQD® nanoparticles induced negligible haemolysis over this concentration range with only 2.6 ± 0.1% discernible (vs. the positive control at 100%) at the highest concentrated of 200 nM. These results are consistent with the data of Helle et al. who also reported negligible haemolysis of mouse blood with cadmium-free QDs, whereas in the same study cadmium-containing CdTeSe/ZnS QDs induced 80–90% haemolysis after exposure for 2 h at 200 nM [41]. Overall, these findings clearly indicate that the bio CFQD® nanoparticles possess good blood biocompatibility.

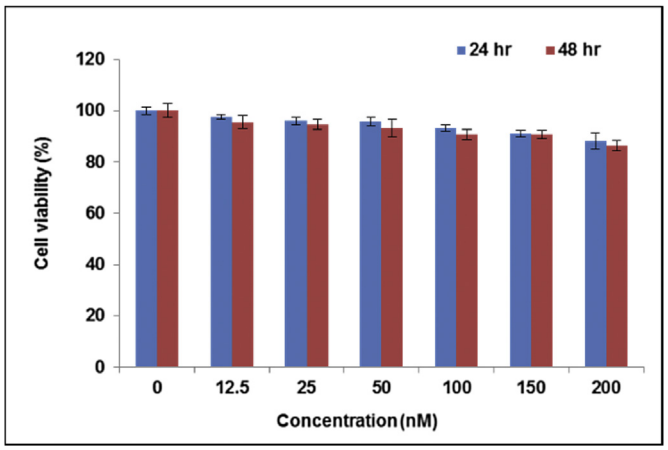

Fig. 2. *In vitro* viability of MCF-7 cells as a function of QDs concentration using the MTT assay. Cells were incubated with bio CFQD® nanoparticles for 24 and 48 h. Data are presented as mean ± standard deviation normalised to untreated control cells. Error bars represent the standard deviation of triplicate experiments.

3.3. Ex vivo macroscopic and microscopic imaging

Macroscopic imaging of QD photoluminescence was carried out on excised lymph nodes. An aqueous solution of the QDs was injected subcutaneously into the left paw of rats and animals were sacrificed 10 min post-injection. The axillary area was exposed, illuminated with a 455 nm light emitting diode (LED), and images were acquired using a CCD camera with 0.1 s integration time. Owing to the high quantum yields and absorbance, the photoluminescence of the QDs in two regional lymph nodes corresponding to left axillary lymph node (LALN) and left thoracic lymph node (LTLN) was readily visible to the naked eye just after injection. As shown in Fig. 3, the QD photoluminescence signal (red colour in Fig. 3B) in the LALN and LTLN was easily detected by 10 min after injection of the QDs similarly to what has been previously reported with other type of QDs [[33,34,41,45,62]). Residual green emission in Fig. 3B is endogenous fluorescence from tissues. These results indicate that following subcutaneous injection, QDs entered the lymphatics and migrated within minutes to the axillary and thoracic lymph nodes. No signal specific to the LNs was detected in control rats injected with PBS.

For the *ex vivo* photoluminescence images, the axillary and thoracic lymph nodes were removed. The harvested tissues were illuminated with a 455 nm LED lamp and images were acquired using a CCD camera. Fig. 4 shows the *ex vivo* photoluminescence images of ALN and TLN at 4 h, 48 h and 5 days post-injection. Bright photoluminescence signal of QDs was detected from ALN and TLN at each of the imaging time points. There was negligible photoluminescence signal in the lymph nodes of rats injected with PBS (data not shown).

Cryosection microscopy of the harvested lymph nodes further confirmed the uptake of the QDs in ALN and TLN. Tissue sections were imaged with a fluorescence microscope. Fig. 5 shows a series of cryosections from ALN and TLN in control and QD-injected rats at various times post-injection, imaged quantitatively using the same detection sensitivity. Compared to the control rats, QD-administered rats exhibited a distinct photoluminescence signal at all post-injection times up to 10 days in both axillary and thoracic lymph nodes. On the same scale, specimens from control animals showed negligible autofluorescence. The images obtained show that QDs remained photoluminescent for as long as 10 days. The QDs must have remained relatively intact to retain detectable photoluminescence signal over such a long period of time.

Fig. 6 displays microscopic images of a cryosection taken from an ALN at 5 min post-injection using 30 pmol/g, and then counterstained using H&E. The results revealed that QDs were mainly localised in the subcapsular sinuses and trabecular regions. The subcapsular sinus is the most likely location of a metastatic carcinoma in a lymph node. These findings are in agreement with other studies where analyses of the resected tissues showed that QDs were confined to the outermost rim of the lymph node [34,63].

3.4. In vivo biodistribution

It is important to understand the pharmacokinetic of QDs before their translation into clinical use. In our study ICP-MS was used to quantify the pharmacokinetics by measuring the indium (In) content in selected organs and serum. A dose of 30 pmol/g was injected subcutaneously into the paw of rats; tissue samples were taken at 1 h, 4 h, 24 h, 72 h, 10 days, 30 days, 60 days and 90 days after QD administration. The concentration of indium in digested tissues was determined using ICP-MS. 1 hr post-injection the indium content in the left axillary lymph node (LALN) and left thoracic lymph node (LTLN) was found to be 86 μg In/g tissue and 63 μg In/g tissue respectively (Fig. 7). The indium concentration in both lymph nodes increased gradually and reached a peak at 24 h post-injection (130 μg In/g tissue and 127 μg In/g tissue for LALN and LTLN respectively). The increase in indium concentration in the lymph nodes following the injection was consistent with the decrease of indium at the injection site in the same time span as the QDs migrated from the injection site through the lymphatic duct system to regional lymph nodes. After 24 h the lymph node accumulation decreased steadily over time. A two-fold decrease of indium was observed 30 days after injection (54 μg In/g tissue and 51 μg In/g tissue for LALN and LTLN respectively). At 90 days post-injection only a small amount of the indium remained in the LALN and LTLN (24 μg In/g tissue and 19 μg In/g tissue respectively). Residual amounts remained at the site of injection by 3 months post-injection.

It is interesting to note that the time-dependence data of the indium content at the injection site, and lymph nodes are similar to those of the Helle et al. study [41], using $CuInS_2$/ZnS QDs encapsulated in PEG. In our study, QDs with PEG grafted to the surface are also used which may explain the similar characteristics, although at longer times owing to degradation the indium content may not necessarily correspond to QD concentration.

Trace quantities of indium were detected in the liver (8.8 μg In/g tissue) and spleen (6 μg In/g tissue) at 1 h post-injection (Fig. 8). Afterwards, the concentration of the indium in both organs increased slightly and reached the peak at 24 h (16 μg In/g tissue and 12 μg In/g tissue for liver and spleen respectively), but this is still an order of magnitude lower than levels found in the lymph nodes. After 24 h the indium concentration in the liver and spleen started to decrease over time. By 90 days, the quantity of indium in the liver had reduced by more than 90% (16.6 μg In/g tissue vs. 1.51 μg In/g tissue, Fig. 8) suggesting hepatobiliary elimination was taking place. Small quantities of indium were detected in kidney which could be due to excretion of QDs from urinary tract in addition to hepatobiliary pathway, but at the longer times the detection of indium is more likely to be due to smaller breakdown products. The hydrodynamic diameter of the QDs although relatively small for water-soluble QDs is too large for efficient urinary excretion according to studies of Choi et al. [64].

Overall, the results show that subcutaneously injected QDs in the paw mainly accumulated in the regional lymph nodes with negligible accumulation in the liver and spleen thus decreasing the likelihood of QD toxicity. As evident from Fig. 8 negligible quantities of indium were detected in all other tissues with no significant trend (thymus, lungs, heart, kidneys, colon). Trace quantities of indium in serum samples at all-time points was also detected.

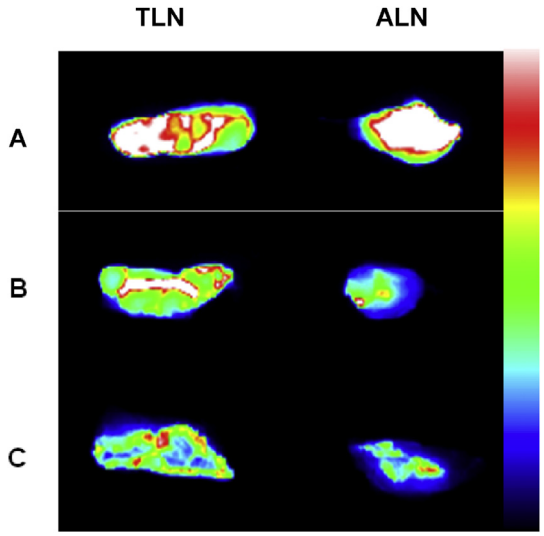

Fig. 4. *Ex vivo* imaging of freshly harvested axillary and thoracic lymph nodes following subcutaneous administration of QDs at 30 pmol/g, at 4 h, 48 h and 5 days post-injection. The axillary lymph node (ALN) and thoracic lymph node (TLN) were illuminated with a 455 nm LED lamp for 0.1 s and images were obtained using a CCD camera. A: 4 h post-injection; B: 48 h post-injection; C: 5 days post-injection. False colour bar scale with blue corresponding to lower intensity.

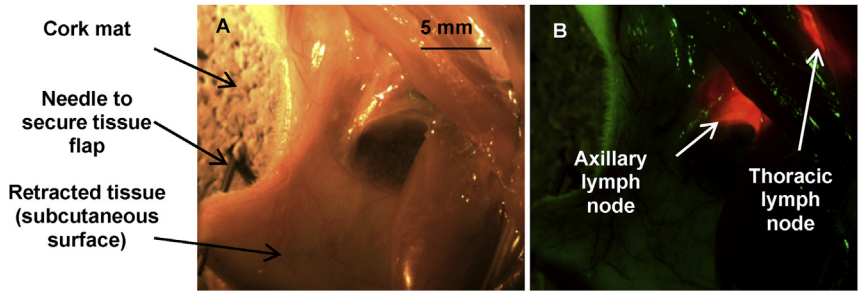

Fig. 3. (A) Colour and (B) photoluminescence image of retracted armpit area following QD administration. QDs were injected subcutaneously into the left paw and the rat was sacrificed 10 min post-injection. Tissues were illuminated with a collimated LED lamp with peak emission at 455 nm (acquisition time: 0.1 s) and the QDs photoluminescence signal was recorded using a colour CCD camera. The green emission in (B) corresponds to tissue autofluorescence, and the red to the QDs photoluminescence in axillary and thoracic lymph nodes.

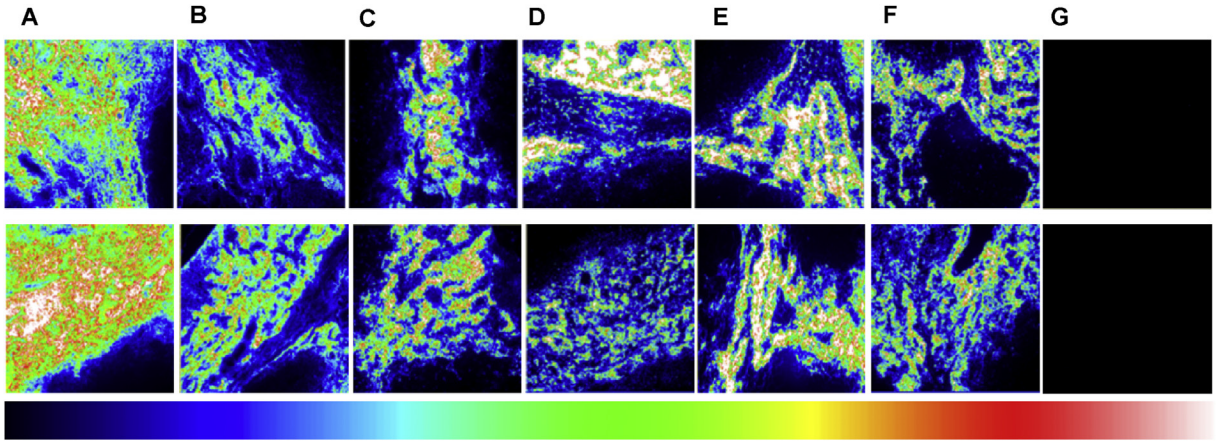

Fig. 5. Photoluminescence microscopy images of cryosections taken from rat axillary (ALN), thoracic (TLN) lymph nodes and control images (G). Top row shows distribution of QDs in axillary lymph node (ALN) and the bottom row displays QDs distribution in thoracic lymph node (TLN) at various time intervals post-injection: (A): 5 min, (B): 1 h, (C): 4 h, (D): 48 h, (E): 5 days and (F): 10 days. G: images from the control rats without QDs injection; image scale: 500 × 500 μm. False colour bar scale with blue corresponding to lower intensity.

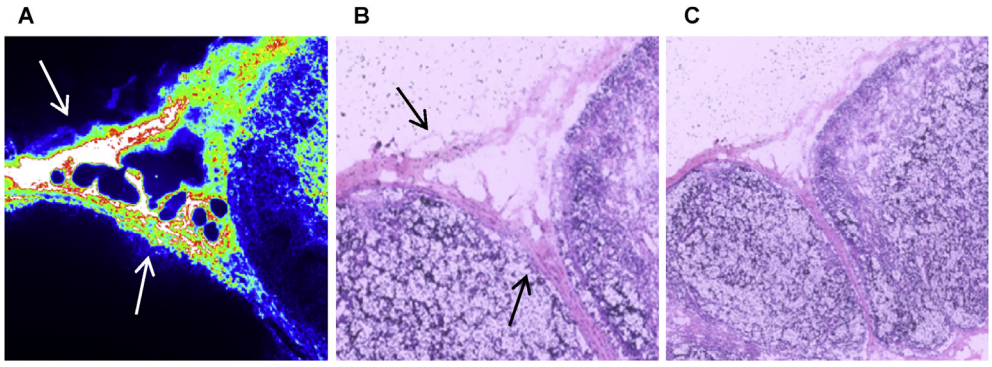

Fig. 6. Photoluminescence (A) image (250 × 250 μm) and corresponding H & E stained image (B) and lower power image (C) of same field from a cryosection of rat axillary lymph node 5 min after QDs injection. High intensities are evident in the subcapsular sinuses (at the top) and trabecular regions (at the left) as shown by the arrows.

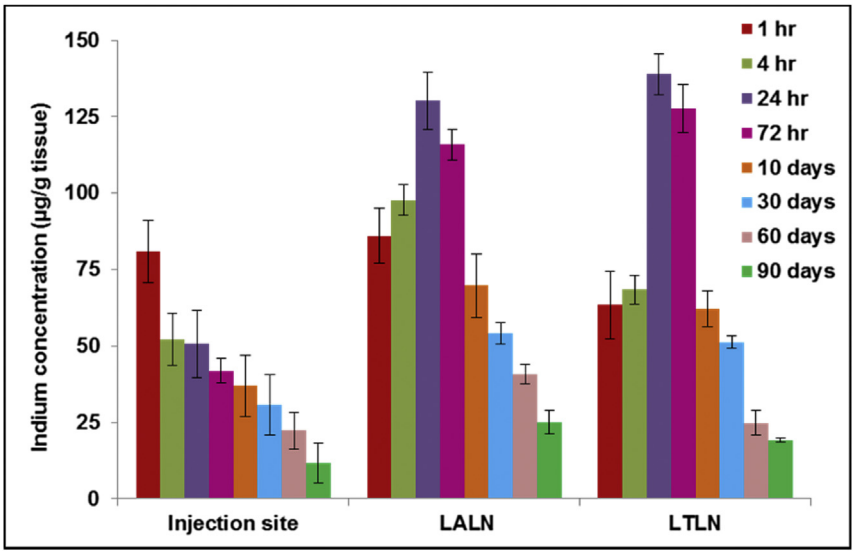

Fig. 7. Quantitative analysis of biodistribution of QDs in rats using ICP-MS. Rats were injected subcutaneously at a concentration of 30 pmol/g of body weight. The indium content in left axillary lymph node (LALN), left thoracic lymph node (LTLN) and injection sites were quantified using ICP-MS and were expressed as the quantity of indium (in μg) per gram of tissue. Data are mean ± SD (n = 3 per group).

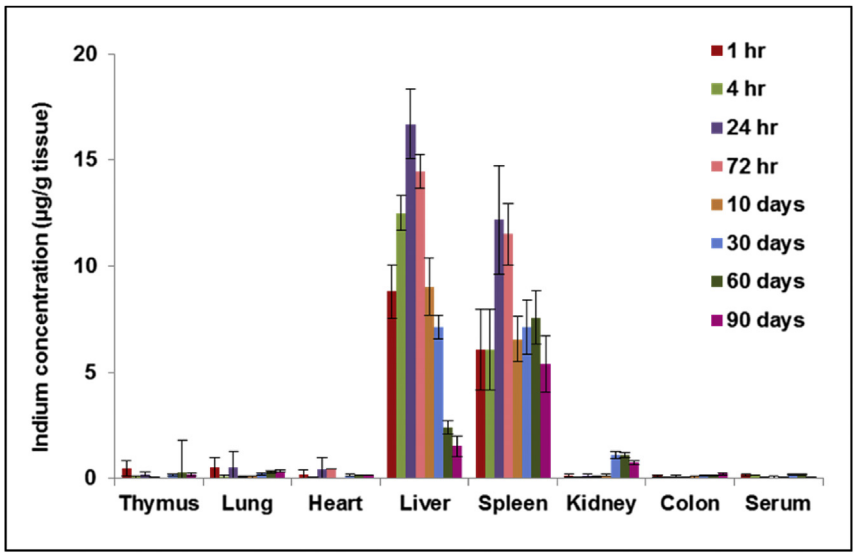

Fig. 8. Biodistribution of QDs in various tissues and serum in rats as a function of post-injection time. Rats were injected subcutaneously with QDs at a concentration of 30 pmol/g body weight. The indium content in organs and serum was quantified using ICP-MS using ICP-MS and were expressed as the quantity of indium (in µg) per gram of tissue or per millilitre of blood. Data are mean ± SD (n = 3 per group).

3.5. *Ex vivo fluorescence lifetime imaging (FLIM)*

To investigate whether uptake into tissue perturbed the photophysical properties of the QDs, we measured the photoluminescence lifetime in *ex vivo* axillary and thoracic lymph nodes using the fluorescence lifetime imaging technique (FLIM) incorporating time-correlated single photon counting (TCSPC) [65,66]. For these measurements, a diode laser with a variable repetition rate was used to enable the adjustment of the time window to collect the entire decay before re-exciting the sample [67].

QDs were injected subcutaneously into the paw of rats, as described previously for the *ex vivo* imaging studies. Animals were sacrificed 10 min post-injection and the LALN and LTLN were removed for the imaging measurements. Excitation of the QDs was carried out using a picosecond laser diode at 470 nm. Fig. 9 shows a lifetime image of a rat thoracic lymph node and mean lifetime histogram. The area images correspond to the subcapsular sinuses and trabecular regions where there is high accumulation of the QDs as shown in Fig. 6.

Biexponential decay analysis of the time-resolved QD photoluminescence intensity (I_t) was carried out using the equation, $I_t = A_1\exp(-t/\tau_1) + A_2\exp(-t/\tau_2) + B$, where A and τ are the fractional amplitude and lifetime, and B is the background; in view of the FLIM photon statistics, the use of more complex decay models in a single pixel is not statistically justified.

Biexponential fitting of the whole-field LALN data gave a major short lifetime component of $\tau_1 = 23$ ns with a large pre-exponential factor or amplitude of 0.87, and a long lifetime component of $\tau_2 = 142$ ns with lower amplitude (Table 1). For the LTLN, the major short and long lifetimes were 20 and 120 ns respectively. The amplitude weighted mean lifetimes for the LALN and LTLN are 39 and 35 ns respectively [68]. These values are close to the amplitude weighted mean lifetime of the QDs measured in aqueous solution (0.01 M PBS, pH 7.4) at 41 ns. The similarity in the emission lifetimes suggests that no significant photoluminescence quenching occurs for the QDs when present in the lymph nodes, although the value observed for the thoracic sample is about 10% lower than for the QD solution. As far as we are aware this is the first study to

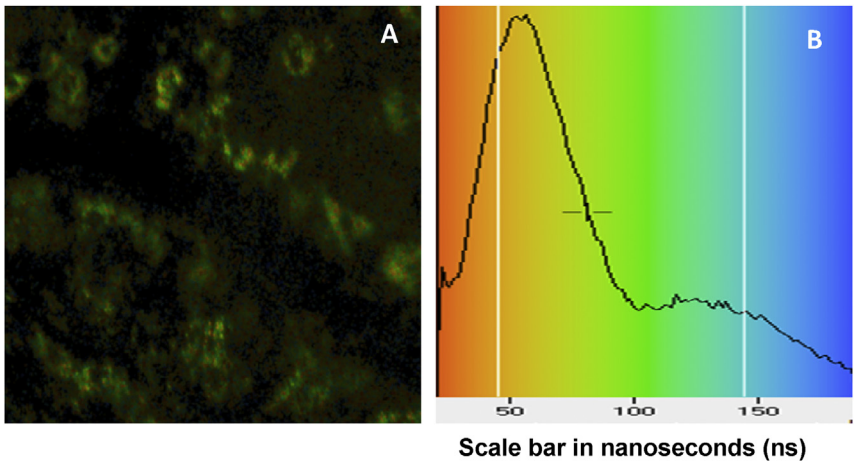

Fig. 9. FLIM image (A) of a rat thoracic lymph node (238 × 238 µm) and (B) mean lifetime histogram with false colour scale in ns. Images were taken following subcutaneous injection of QDs at 30 pmol/g of body weight.

Table 1
Photoluminescence lifetime components of QDs in axillary and thoracic lymph nodes compared to aqueous solution (100 nM).

QDs photoluminescence lifetime τ/ns and fractional amplitudes (A)	τ_1 (A_1)	τ_2 (A_2)
Aqueous solution	26 (0.85)	132 (0.15)
Axillary lymph node	23 (0.87)	142 (0.13)
Thoracic lymph node	20 (0.85)	120 (0.15)

produce such comparison. The relatively long photoluminescence lifetime of QDs could also provide a means to distinguish the QDs photoluminescence from shorter-lived autofluorescence using time-gated imaging.

4. Conclusions

QD nanoparticles have several unique properties which are potentially useful for clinical applications such as intraoperative SLN mapping. However, most of the engineered core/shell QDs contain regulated heavy metals which would severely restrict their clinical use. Therefore, in the present study we have investigated new cadmium-free QDs (bio CFQD® nanoparticles) which can be prepared in bulk with high photoluminescence quantum yields. These quantum dots are surface functionalised with a biocompatible coating to confer water solubility. We examined their potential for *in vivo* SLN mapping using a regional lymph node animal model.

These bright and photostable indium-based QDs are soluble and colloidally stable in water. Using photoluminescence imaging we showed that the bio CFQD® nanoparticles, when injected subcutaneously into paw of rats, accumulated preferentially in two regional LNs draining the thoracic mammary fat pads in rats. The biodistribution study using chemical extraction revealed that with subcutaneous injection of QDs into the paw, retention is strongly confined to regional lymph nodes since only trace quantities of QDs were detected in other organs. Localisation took place within minutes of injection and photoluminescence was stable for an extended period unlike blue dyes which drain relatively quickly from lymph nodes. This observation could be advantageous since false positive samples related to the fast migration of the dyes across the lymphatic channel can be avoided and the extended retention is logistically easier to deal with in a clinical setting.

Furthermore the engineered bio CFQD® nanoparticles do not contain any Class A elements (Cd, Pb and Hg) therefore their low intrinsic toxicity may further promote their biomedical applications. However additional work will be needed to study long-term toxicity effects of bio CFQD® nanoparticles.

Acknowledgments

This work was supported by Innovate UK (grant numbers 107017 and 101875) and the UK Medical Research Council under the Biomedical Catalyst scheme. We are grateful for project management overseen by Dr Lesley Smith, Joe Broughton for help with the analytical studies, and Andy Cakebread with the ICP-MS measurements.

References

[1] S.A. Eccles, D.R. Welch, Metastasis: recent discoveries and novel treatment strategies, Lancet 369 (2007) 1742–1757.
[2] S.D. Nathanson, Insights into the mechanisms of lymph node metastasis, Cancer 98 (2003) 413–423.
[3] A.D. Purushotham, S. Upponi, M.B. Klevesath, L. Bobrow, K. Millar, J.P. Myles, et al., Morbidity after sentinel lymph node biopsy in primary breast cancer: results from a randomized controlled trial, J. Clin. Oncol. 23 (2005) 4312–4321.
[4] D.C. Budd, R.C. Cochran, D.L. Sturtz, W.J. Fouty Jr., Surgical morbidity after mastectomy operations, Am. J. Surg. 135 (1978) 218–220.
[5] R.E. Mansel, L. Fallowfield, M. Kissin, A. Goyal, R.G. Newcombe, J.M. Dixon, et al., Randomized multicenter trial of sentinel node biopsy versus standard axillary treatment in operable breast cancer: the ALMANAC Trial, J. Natl. Cancer Inst. 98 (2006) 599–609.
[6] R.M. Cabanas, An approach for the treatment of penile carcinoma, Cancer 39 (1977) 456–466.
[7] E.A. Gould, T. Winship, P.H. Philbin, H.H. Kerr, Observations on a "sentinel node" in cancer of the parotid, Cancer 13 (1960) 77–78.
[8] M.R. Keshtgar, P.J. Ell, Clinical role of sentinel-lymph-node biopsy in breast cancer, Lancet Oncol. 3 (2002) 105–110.
[9] J.J. Albertini, G.H. Lyman, C. Cox, T. Yeatman, L. Balducci, N. Ku, et al., Lymphatic mapping and sentinel node biopsy in the patient with breast cancer, JAMA 276 (1996) 1818–1822.
[10] S.K. Somasundaram, D.W. Chicken, M.R. Keshtgar, Detection of the sentinel lymph node in breast cancer, Br. Med. Bull. 84 (2007) 117–131.
[11] S.K. Somasundaram, D.W. Chicken, W.A. Waddington, J. Bomanji, P.J. Ell, M.R. Keshtgar, Sentinel node imaging in breast cancer using superficial injections: technical details and observations, Eur. J. Surg. Oncol. 35 (2009) 1250–1256.
[12] A. Goyal, R.G. Newcombe, A. Chhabra, R.E. Mansel, Factors affecting failed localisation and false-negative rates of sentinel node biopsy in breast cancer–results of the ALMANAC validation phase, Breast Cancer Res. Treat. 99 (2006) 203–208.
[13] A.E. Giuliano, D.M. Kirgan, J.M. Guenther, D.L. Morton, Lymphatic mapping and sentinel lymphadenectomy for breast cancer, Ann. Surg. 220 (1994) 391–398.
[14] L. Barthelmes, A. Goyal, R.G. Newcombe, F. McNeill, R.E. Mansel, Adverse reactions to patent blue V dye - the NEW START and ALMANAC experience, Eur. J. Surg. Oncol. 36 (2010) 399–403.
[15] D. Albo, J.D. Wayne, K.K. Hunt, T.F. Rahlfs, S.E. Singletary, F.C. Ames, et al., Anaphylactic reactions to isosulfan blue dye during sentinel lymph node biopsy for breast cancer, Am. J. Surg. 182 (2001) 393–398.
[16] G. Mariani, L. Moresco, G. Viale, G. Villa, M. Bagnasco, G. Canavese, et al., Radioguided sentinel lymph node biopsy in breast cancer surgery, J. Nucl. Med. 42 (2001) 1198–1215.
[17] D.N. Krag, D.L. Weaver, J.C. Alex, J.T. Fairbank, Surgical resection and radiolocalization of the sentinel lymph node in breast cancer using a gamma probe, Surg. Oncol. 2 (1993) 335–339.
[18] Y. Minamiya, M. Ito, Y. Katayose, H. Saito, K. Imai, Y. Sato, et al., Intraoperative sentinel lymph node mapping using a new sterilizable magnetometer in patients with nonsmall cell lung cancer, Ann. Thorac. Surg. 81 (2006) 327–330.
[19] T. Nakagawa, Y. Minamiya, Y. Katayose, H. Saito, K. Taguchi, H. Imano, et al., A novel method for sentinel lymph node mapping using magnetite in patients with non-small cell lung cancer, J. Thorac. Cardiovasc. Surg. 126 (2003) 563–567.
[20] M. Shiozawa, A.T. Lefor, Y. Hozumi, K. Kurihara, N. Sata, Y. Yasuda, et al., Sentinel lymph node biopsy in patients with breast cancer using superparamagnetic iron oxide and a magnetometer, Breast Cancer 20 (2013) 223–229.
[21] M. Douek, J. Klaase, I. Monypenny, A. Kothari, K. Zechmeister, D. Brown, et al., Sentinel node biopsy using a magnetic tracer versus standard technique: the SentiMAG Multicentre Trial, Ann. Surg. Oncol. 21 (2014) 1237–1245.
[22] B.E. Schaafsma, J.S. Mieog, M. Hutteman, J.R. van der Vorst, P.J. Kuppen, C.W. Lowik, et al., The clinical use of indocyanine green as a near-infrared fluorescent contrast agent for image-guided oncologic surgery, J. Surg. Oncol. 104 (2011) 323–332.
[23] A. Liebert, P. Sawosz, D. Milej, M. Kacprzak, W. Weigl, M. Botwicz, et al., Assessment of inflow and washout of indocyanine green in the adult human brain by monitoring of diffuse reflectance at large source-detector separation, J. Biomed. Opt. 16 (2011) 0460111–0460117.
[24] K. Motomura, H. Inaji, Y. Komoike, T. Kasugai, S. Noguchi, H. Koyama, Sentinel node biopsy guided by indocyanine green dye in breast Cancer patient, JJCO 29 (1999) 604–607.
[25] E.M. Sevick-Muraca, R. Sharma, J.C. Rasmussen, M.V. Marshall, J.A. Wendt, H.Q. Pham, et al., Imaging of lymph flow in breast cancer patients after microdose administration of a near-infrared fluorophore: feasibility study, Radiology 246 (2008) 734–741.
[26] M. Green, Semiconductor quantum dots as biological imaging agents, Angew. Chemie-International Ed. 43 (2004) 4129–4131.
[27] C.E. Probst, P. Zrazhevskiy, V. Bagalkot, X. Gao, Quantum dots as a platform for nanoparticle drug delivery vehicle design, Adv. Drug Deliv. Rev. 65 (2013) 703–718.
[28] E. Cassette, M. Helle, L. Bezdetnaya, F. Marchal, B. Dubertret, T. Pons, Design of new quantum dot materials for deep tissue infrared imaging, Adv. Drug Deliv. Rev. 65 (2013) 719–731.
[29] E. Yaghini, F. Giuntini, I.M. Eggleston, K. Suhling, A.M. Seifalian, A.J. MacRobert, Fluorescence lifetime imaging and FRET-induced intracellular redistribution of Tat-Conjugated quantum dot nanoparticles through interaction with a phthalocyanine photosensitiser, Small 10 (2014) 782–792.
[30] U. Resch-Genger, M. Grabolle, S. Cavaliere-Jaricot, R. Nitschke, T. Nann,

Quantum dots versus organic dyes as fluorescent labels, Nat. Methods 5 (2008) 763–775.
[31] K.D. Wegner, N. Hildebrandt, Quantum dots: bright and versatile *in vitro* and *in vivo* fluorescence imaging biosensors, Chem. Soc. Rev. 44 (2015) 4792–4834.
[32] L.W. Wang, C.W. Peng, C. Chen, Y. Li, Quantum dots-based tissue and *in vivo* imaging in breast cancer researches: current status and future perspectives, Breast Cancer Res. Treat. 151 (2015) 7–17.
[33] B. Ballou, L.A. Ernst, S. Andreko, T. Harper, J.A. Fitzpatrick, A.S. Waggoner, et al., Sentinel lymph node imaging using quantum dots in mouse tumor models, Bioconjug Chem. 18 (2007) 389–396.
[34] S. Kim, Y.T. Lim, E.G. Soltesz, A.M. De Grand, J. Lee, A. Nakayama, et al., Near-infrared fluorescent type II quantum dots for sentinel lymph node mapping, Nat. Biotechnol. 22 (2004) 93–97.
[35] C.P. Parungo, Y.L. Colson, S.W. Kim, S. Kim, L.H. Cohn, M.G. Bawendi, et al., Sentinel lymph node mapping of the pleural space, Chest 127 (2005) 1799–1804.
[36] C.P. Parungo, S. Ohnishi, S.W. Kim, S. Kim, R.G. Laurence, E.G. Soltesz, et al., Intraoperative identification of esophageal sentinel lymph nodes with near-infrared fluorescence imaging, J. Thorac. Cardiovasc Surg. 129 (4) (2005) 844–850.
[37] E.G. Soltesz, S. Kim, R.G. Laurence, A.M. DeGrand, C.P. Parungo, D.M. Dor, et al., Intraoperative sentinel lymph node mapping of the lung using near-infrared fluorescent quantum dots, Ann. Thorac. Surg. 79 (2005) 269–277.
[38] E.G. Soltesz, S. Kim, S.W. Kim, R.G. Laurence, A.M. De Grand, C.P. Parungo, et al., Sentinel lymph node mapping of the gastrointestinal tract by using invisible light, Ann. Surg. Oncol. 13 (2006) 386–396.
[39] H. Kobayashi, Y. Hama, Y. Koyama, T. Barrett, C.A. Regino, Y. Urano, et al., Simultaneous multicolor imaging of five different lymphatic basins using quantum dots, Nano Lett. 7 (2007) 1711–1716.
[40] J.P. Zimmer, S.W. Kim, S. Ohnishi, E. Tanaka, J.V. Frangioni, M.G. Bawendi, Size series of small indium arsenide-zinc selenide core-shell nanocrystals and their application to *in vivo* imaging, J. Am. Chem. Soc. 128 (2006) 2526–2527.
[41] M. Helle, E. Cassette, L. Bezdetnaya, T. Pons, A. Leroux, F. Plenat, et al., Visualisation of sentinel lymph node with indium-based near infrared emitting quantum dots in a murine metastatic breast cancer model, PLoS One 7 (2012) e44433.
[42] J. Fan, Y. Sun, S. Wang, Y. Li, X. Zeng, Z. Cao, et al., Inhibition of autophagy overcomes the nanotoxicity elicited by cadmium-based quantum dots, Biomaterials 78 (2015) 102–114.
[43] J. Lovric, S.J. Cho, F.M. Winnik, D. Maysinger, Unmodified cadmium telluride quantum dots induce reactive oxygen species formation leading to multiple organelle damage and cell death, Chem. Biol. 12 (2005) 1227–1234.
[44] W.E. Smith, J. Brownell, C.C. White, Z. Afsharinejad, J. Tsai, X. Hu, et al., *In vitro* toxicity assessment of amphiphillic polymer-coated CdSe/ZnS quantum dots in two human liver cell models, ACS Nano 6 (2012) 9475–9484.
[45] T. Pons, E. Pic, N. Lequeux, E. Cassette, L. Bezdetnaya, F. Guillemin, et al., Cadmium-free $CuInS_2$/ZnS quantum dots for sentinel lymph node imaging with reduced toxicity, ACS Nano 4 (2010) 2531–2538.
[46] K. Ding, L. Jing, C. Liu, Y. Hou, M. Gao, Magnetically engineered Cd-free quantum dots as dual-modality probes for fluorescence/magnetic resonance imaging of tumors, Biomaterials 35 (2013) 1608–1617.
[47] J. Gao, K. Chen, R. Xie, J. Xie, S. Lee, Z. Cheng, et al., Ultrasmall near-infrared non-cadmium quantum dots for *in vivo* tumor imaging, Small 6 (2010) 256–261.
[48] V. Brunetti, H. Chibli, R. Fiammengo, A. Galeone, M.A. Malvindi, G. Vecchio, et al., InP/ZnS as a safer alternative to CdSe/ZnS core/shell quantum dots: *in vitro* and *in vivo* toxicity assessment, Nanoscale 5 (2013) 307–317.
[49] D.J. Bharali, D.W. Lucey, H. Jayakumar, H.E. Pudavar, P.N. Prasad, Folate-receptor-mediated delivery of InP quantum dots for bioimaging using confocal and two-photon microscopy, J. Am. Chem. Soc. 127 (2005) 11364–11371.
[50] K.T. Yong, H. Ding, I. Roy, W.C. Law, E.J. Bergey, A. Maitra, et al., Imaging pancreatic cancer using bioconjugated InP quantum dots, ACS Nano 3 (2009) 502–510.
[51] S.W. Kim, J.P. Zimmer, S. Ohnishi, J.B. Tracy, J.V. Frangioni, M.G. Bawendi, Engineering InAs(x)P(1-x)/InP/ZnSe III-V alloyed core/shell quantum dots for the near-infrared, J. Am. Chem. Soc. 127 (2005) 10526–10532.
[52] E. Cassette, T. Pons, C. Bouet, L. Bezdetnaya, F. Marchal, B. Dubertret, Synthesis and characterization of near-infrared Cu-In-Se/ZnS core/shell quantum dots for *in vivo* imaging, Chem. Mater. 22 (2010) 6117–6124.
[53] Pikett N, Daniels S, Mushtaq I, inventors; Preparation of Nanoparticle Materials. US Patent 7,588,828.7,588,828 B2. 2009.
[54] Naasani I, inventor; Surface Modified Nanoparticles. US Patent 9,115,097.9,115,097. 2015.
[55] H.S. Choi, B.I. Ipe, P. Misra, J.H. Lee, M.G. Bawendi, J.V. Frangioni, Tissue- and organ-selective biodistribution of NIR fluorescent quantum dots, Nano Lett. 9 (2009) 2354–2359.
[56] G. Hong, J.T. Robinson, Y. Zhang, S. Diao, A.L. Antaris, Q. Wang, et al., *In vivo* fluorescence imaging with Ag_2S quantum dots in the second near-infrared region, Angew. Chem. Int. Ed. Engl. 51 (2012) 9818–9821.
[57] M.A. Dobrovolskaia, J.D. Clogston, B.W. Neun, J.B. Hall, A.K. Patri, S.E. McNeil, Method for analysis of nanoparticle hemolytic properties *in vitro*, Nano Lett. 8 (2008) 2180–2187.
[58] H. Huang, W. Lai, M. Cui, L. Liang, Y. Lin, Q. Fang, et al., An evaluation of blood compatibility of silver nanoparticles, Sci. Rep. 6 (2016) 1–15.
[59] W.T. Al-Jamal, K.T. Al-Jamal, A. Cakebread, J.M. Halket, K. Kostarelos, Blood circulation and tissue biodistribution of lipid–quantum dot (L-QD) hybrid vesicles intravenously administered in mice, Bioconjug Chem. 20 (2009) 1696–1702.
[60] S.J. Soenen, B.B. Manshian, T. Aubert, U. Himmelreich, J. Demeester, S.C. De Smedt, et al., Cytotoxicity of cadmium-free quantum dots and their use in cell bioimaging, Chem. Res. Toxicol. 27 (2014) 1050–1059.
[61] P. Rivera-Gil, A.D. Jimenez de, V. Wulf, B. Pelaz, P.P. del, Y. Zhao, et al., The challenge to relate the physicochemical properties of colloidal nanoparticles to their cytotoxicity, Acc. Chem. Res. 46 (2013) 743–749.
[62] E. Pic, T. Pons, L. Bezdetnaya, A. Leroux, F. Guillemin, B. Dubertret, et al., Fluorescence imaging and whole-body biodistribution of near-infrared-emitting quantum dots after subcutaneous injection for regional lymph node mapping in mice, Mol. Imaging Biol. 12 (2010) 394–405.
[63] N.V. Gopee, D.W. Roberts, P. Webb, C.R. Cozart, P.H. Siitonen, A.R. Warbritton, et al., Migration of intradermally injected quantum dots to sentinel organs in mice, Toxicol. Sci. 98 (2007) 249–257.
[64] H.S. Choi, W. Liu, P. Misra, E. Tanaka, J.P. Zimmer, I.B. Itty, et al., Renal clearance of quantum dots, Nat. Biotechnol. 25 (2007) 1165–1170.
[65] K. Suhling, P.M.W. French, D. Phillips, Time-resolved fluorescence microscopy, Photochem. Photobiol. Sci. 4 (2005) 13–22.
[66] K. Suhling, L.M. Hirvonen, J.A. Levitt, P. Chung, C. Tregidgo, A. Le Marois, et al., Fluorescence lifetime imaging (FLIM): basic concepts and some recent developments, Med. Photonic 27 (2015) 3–40.
[67] A. Shivalingam, A. Le Marois, Izquierdo, M.A. Le, A. Vysniauskas, K. Suhling, M.K. Kuimova, et al., The interactions between a small molecule and G-quadruplexes are visualized by fluorescence lifetime imaging microscopy, Nat. Commun. 6 (2015) 1–10.
[68] A. Sillen, Y. Engelborghs, The correct use of “average” fluorescence parameters, Photochem Photobiol. 68 (2008) 475–486.